

A modeling and migration study of fault shadows: A synthetic example

Sitamai W. Ajiduah and Gary F. Margrave

This report presents a study that uses 2D finite difference modeling and a one-way wave equation depth migration method to investigate weak illuminations in footwall reflectors. I examined the quality of footwall imaging from poststack and prestack migrations with exact model and created approximate models using an iterative method from an initial unfaulted (flat) model. Appearances of fault shadow effect were seen in the geologic model as time pull and sags, in poststack time migrations as distorted reflections which appeared as sub-seismic fault. In the depth migrated images, they occurred as anticlines and synclines which may be false or real. We observed a confined section of the footwall was poorly illuminated. Results from the prestack depth migrations was quite significant with improved imaging. The velocity model time anomalies are the results of the truncation of the overlying stratigraphy by the fault throw causing an abrupt velocity contrast across the fault. Seismic rays undergo ray bending and experience travelttime distortions as it propagates across fault truncations. In addition, the presence of the dipping faults in the model will create some non-hyperbolic reflections which will frustrate poststack migration efforts. The poor images in poststack time migration implies that events are migrated to their incorrect positions in vertical time with a Dix-based RMS velocity transformation that is suboptimal. The inadequacies of poststack depth migrations in perfectly imaging footwall reflections can also be attributed to the dip-dependence effect of normal moveout. NMO and stacking of events along hyperbolas without prior dip moveout correction will cause apparent disruptions and smeared reflections. A better imaging solution is obtained from the prestack depth migrations which showed improved and continuous footwall reflections without seismic artifacts. In conclusion, fault shadow is a velocity and wave propagation problem and requires good understanding of the faulted environment and velocities.

INTRODUCTION

This study presents a synthetic study that uses 2D finite difference methods for modeling and phase-shift-plus-interpolation (PSPI) depth migration to investigate weak illumination behind major fault boundaries. These poor illuminations are sometimes called zones of unreliable seismic imaging (Hardwick et. al., 2013). They mostly occur in steeply dipping complex geologic structures like the flanks of subsalts and in the footwalls of major fault boundaries. Also called fault shadow zones, they pose a risk for potential exploration and development and can prevent exploration for deep resource plays. The primary cause of fault shadow is attributed to the presence of rapidly varying lateral velocity contrast across the fault zone (Stuart, 1999, Birdus, 2007). Typical examples of reported cases are in the boundary fault of South Texas and the Gulf of Mexico, Tertiary graben of onshore Poland, the permafrost region of Siberia (Stuart, 1999), and the regressive delta in the Gulf of Guinea (Schultz, 1999). The main aim of this study is to understanding the causes of fault shadows in typical seismic datasets acquired in areas which large growth fault and complex faulting environments.

Another objective of this study is to determine the effectiveness of seismic migration in resolving problems of this type. The PSPI method was proposed by Gazdag and Sguazzero in 1984. It is a class of phase-shift wavefield continuation method that is Fourier based. The PSPI wavefield-continuation methods belong to a one-way wave operator class (Ferguson and Margrave 2005, Bancroft, 2007) that is capable of handling strong velocity gradients but cannot migrate overturned reflections or multiples. I used the classic PSPI method in 2-D poststack migration and 2-D prestack common-shot migration as applied to zero-offset synthetic datasets as well as the multi-offset shot records.

The outline of this paper is as follows: First, I will briefly review the principles of finite difference, phase-shift-plus-interpolation and downward continuation imaging conditions. Secondly, I will describe the methodology used and lastly discuss the results and findings. The first step is the designing of the framework for building a geologic fault model consisting of a sequence of three listric normal faults that interrupt a stratified sequence defined by a P-wave velocities from sonic logs. I then generated synthetic datasets, from finite difference, sufficient to study both poststack and prestack imaging. For imaging, I used both poststack and prestack PSPI. In the former case I used the method as both a time migration and a depth migration. In the second case I only examined prestack depth migration due to reduce computational costs. I examined the quality of imaging with both exact and approximate models and created an iterative method to build a model from an initial unfaulted (flat) model.

THEORY

In this section I shall briefly review the fundamental principle behind the 2D finite difference modeling and PSPI migration employed in this work.

Finite Difference Modeling

This is useful for understanding imaging problems and provides a direct solution by solving the wave equation numerically as a set of partial differential equations with the initial and boundary conditions. A number of techniques based on finite differencing have been discussed in literature (Krebs et. al., 1994, Youzwishen and Margrave, 1999, Manning and Margrave, 1999) for the computation of synthetic seismograms from simple to complex geologic models for isotropic and anisotropic acoustic and elastic wave scenarios. The 2D scalar wave equation is

$$\frac{\partial^2 \Psi(x, z, t)}{\partial t^2} = v^2(x, z) \nabla^2 \Psi(x, z, t), \quad 1$$

where $\Psi(x, z, t)$ is the pressure wavefield propagating in a medium with true velocity v , with x , the horizontal space coordinate, z , the depth, t , is time and ∇^2 the laplacian is given by:

$$\nabla^2 \Psi = \frac{\partial^2 \Psi}{\partial x^2} + \frac{\partial^2 \Psi}{\partial y^2} + \frac{\partial^2 \Psi}{\partial z^2}, \quad 2$$

The Laplacian operator can be approximated with central difference operators. The approximation employed in this study is the 9 point approximation which gives the fourth-order approximation to the Laplacian operator.

The fourth order approximation is given by Youzwishen and Margrave (1999) as:

$$\nabla^2 \Psi_j^n \approx \frac{-\Psi_j^{n+2} + 16\Psi_j^{n+1} - 30\Psi_j^n + 16\Psi_j^{n-1} - \Psi_j^{n-2}}{12\Delta x^2} + \frac{-\Psi_{j+2}^n + 16\Psi_{j+1}^n - 30\Psi_j^n + 16\Psi_{j-1}^n - \Psi_{j-2}^n}{12\Delta z^2} \quad 3$$

where n is the x coordinate and j is the z coordinate of the grid.

Grid dispersion is the most significant numerical problem. To minimize grid dispersion I discretized the model with fine grid spacing. The grid spacing was set at 5m and equal in x and z direction in order to ensure symmetric performance of the difference operators.

$$\frac{V_{max}\Delta t}{\Delta x} \leq \sqrt{\frac{3}{8}}, \quad 4$$

where V_{max} is the maximum velocity in the model and Δt and Δx temporal are the spatial sampling interval respectively. If this ratio is larger than the quoted value above, the propagation scheme it helps define will not be stable. The time derivative of the scalar wave equation calculated by second order finite difference scheme is:

$$\frac{\partial^2 \Psi}{\partial t^2} = \frac{\Psi(t+\Delta t) - 2\Psi(t) + \Psi(t-\Delta t)}{\Delta t^2}, \quad 5$$

The AFD_EXPLODE and AFD_SHOOTLINE Matlab code in the CREWES toolbox was used to generate the 2D zero offset exploding reflector model and multi-offset shot records for subsequent post stack and prestack migrations. These codes are second order in time and fourth order in space and use explicit time stepping.

All explicit finite difference methods have numerical dispersion and stability issues. To minimize grid dispersion I chose a very small spatial grid size of 5m. Then to ensure stability, I used the known stability condition in equation 4 above to determine a stable time step. Our final seismograms were sampled in time at 4 milliseconds but the time step used was 0.7 milliseconds.

Substituting equation 5 and the 4th order laplacian approximation into the scalar wave equation, we can solve for the wavefield at time = $t + \Delta t$. Given two initial snapshots (wavefield at time t and $t - \Delta t$) we can create the wavefield at time = $t + \Delta t$.

The time stepping equation can be written as:

$$\Phi_j^n(t + \Delta t) \approx \left(\Delta t^2 (V_j^n)^2 \nabla^2 + 2 \right) \Phi_j^n(t) - \Phi_j^n(t - \Delta t), \quad 6$$

Other factor I put into consideration during my acquisition design for maximum resolution is the spatial aliasing criterion.

Phase-Shift-Plus-Interpolation

PSPI migration uses a number of reference velocities to extrapolate the seismic wavefield from one depth to the next. Many different methods of extrapolating wavefields

are present in literatures like Margrave and Ferguson, 1998, Bancroft J.C., 2007. PSPI requires the selection of reference velocities. One approach was presented in Gazdag and Sguazzero (1984). The reference velocities are obtained in terms of the ratio of maximum velocity and minimum velocity at some depth as well as a common ratio for which a geometric progression for reference velocities is formed. Another statistical method for determining the reference velocities was suggested by Bagaini et. al. (1995). These authors suggests that a geometric distribution can produce a good set of reference velocities. Kessinger (1992) mentions that, by empirical testing, a percentage velocity increment of 15% provides a good compromise between accuracy and efficiency. Another standard method calculates a linear distribution of velocities (e.g. Ferguson and Margrave, 2002), which may have an advantage of increasing the accuracy of higher angle wavefield propagation with depth.

The PSPI method consists of phase-shift wavefield continuation with constant reference velocity and interpolation between different wavefields continued with different reference velocities (the Bagaini model is employed in this study). In this method, a time-shift term is first applied to the initial wavefield before downward wavefield continuation. The basis of the PSPI method are (1) a time-shift term applied to the initial wavefield; 2) phase-shift with reference velocities and 3) interpolation between wavefields.

The recorded wavefield $\Psi(x, z = 0, t)$ in the $t-x$ domain is 2D Fourier transformed into $\omega - k_x$ domain to give $\Psi(k_x, z, \omega)$ where ω is the temporal frequency and k_x is the spatial wavenumber. Then wave equation (1) can be solved in the $\omega - k_x$ domain by phase-shift method which gives an analytic solution for wave extrapolation for depth migration with a depth step Δz and assuming constant velocity.

The scalar wave equation in equation 1 above can be factored into two first order equations given as:

$$\left[\frac{\partial}{\partial z} \pm \sqrt{\left(\frac{1}{v^2} \frac{\partial^2}{\partial t^2} - \frac{\partial^2}{\partial x^2} \right)} \right] \Psi = 0, \quad 7$$

For a one way downward continuation, the minus sign is chosen as it represent a wavefield propagating in depth with increasing time. The frequency-domain representation for equation 7 is given as:

$$\left[\frac{\partial}{\partial z} - i \sqrt{\left(\frac{\omega^2}{v^2} - k_x^2 \right)} \right] \psi = 0, \quad 8$$

The solution to the Fourier series of the pressure wavefield is given as:

$$\Psi(x, z, t) = \iint_{x, \omega} \varphi(k_x, z, \omega) \exp i(k_x x - \omega t) dk_x d\omega, \quad 9$$

Equation 9 is the wavefield $\Psi(x, z, t)$ in 2D frequency domain, where ω is radial frequency and k_x is radial wavenumber.

The basic idea of PSPI is to introduce several reference velocities to account for the lateral velocity variation in each extrapolation step and obtain the multi-reference wavefields in the frequency-wavenumber domain. Based on the relationship of the local

velocity and reference velocity, the final migration result is obtained by interpolating the reference wavefields in the frequency-space domain. The basic formulas are:

$$\Psi_0(x, z, \omega) = \Psi(x, z, \omega) \exp i \left(\frac{\omega}{v(x,z)} dz \right), \quad 10$$

and

$$\psi(k_x, z + dz, \omega) = \psi_0(k_x, z, \omega) \exp ik'_z dz, \quad 11$$

where

$$k'_z = \sqrt{\frac{\omega^2}{v_{ref}^2} - k_x^2} - \frac{\omega}{v_{ref}}. \quad 12$$

Usually a range of reference velocities are chosen for each depth step producing a set of reference wavefields. The final result after each depth step is obtained by linearly (in velocity) interpolating the reference wavefields (Bancroft J.C., 2007). Obviously, the choice of the reference velocities is a crucial task for PSPI migration mainly because the cost of PSPI is proportional to the number of reference velocity values used in each extrapolation step. In order to decrease the cost, the adaptive strategy of (Bagaini, 1995) is adopted for the numerical results shown in this chapter. This adaptive strategy of selecting reference velocities not only reduces the cost of PSPI, but it also computes the reference velocities according to the distribution of velocities. More reference velocities will be used when the lateral velocity variation is strong and fewer velocity values will be used when the velocity contrast is small.

Downward Continuation Imaging Condition

The objective is to downward continue the 2D acoustic recorded data, $\Psi(x, z, t = 0)$ to get $\Psi(x, z = 0, t)$. The classic Claerbout (1971) imaging condition is a deconvolution imaging condition where the ratio of the upgoing and downgoing wave fields is used to get a direct estimate of the reflection coefficient. This imaging condition still enforces the same time same place principle, but it normalizes the amplitudes to the incident flux. However, this imaging condition suffers from numerical stability issues when the denominator is small. To circumvent this problem, the deconvolution imaging condition is often modified by cross-correlation.

For poststack data, the reflectivity image is estimated by evoking the $t = 0$ imaging condition $r(x, z) = \psi(x, z, t = 0)$. For prestack data, the upcoming wavefield $\psi_r(x, 0, \omega)^-$ must be downward continued to give $\psi_r(x, z, \omega)^-$, and the downgoing source wavefield at the surface $\psi_s(x, 0, \omega)^+$ must be downward continued to give $\psi_s(x, z, \omega)^+$. The extrapolation operator for the downgoing source field is $\exp i(k_z \Delta z)$, that is $\psi_s(k_z, \Delta z, \omega)^+ = \psi_s(k_z, 0, \omega)^+ \exp i(k_z \Delta z)$; while the downward continuation operator for the data is $\exp i(-k_z \Delta z)$, that is $\psi_r(k_z, \Delta z, \omega)^- = \psi_r(k_z, 0, \omega)^- \exp -i(k_z \Delta z)$. Then the cross-correlation imaging condition is

$$r_{cc}(x, z) = (\psi_s(k_z, \Delta z, \omega)^+)^* \psi_r(k_z, \Delta z, \omega)^- \quad 13$$

where * indicates the complex conjugate. The deconvolution imaging condition is

$$r_{dec}(x, z) = \frac{r_{cc}(x, z)}{(\psi_s(k_z, \Delta z, \omega)^+)^* \psi_s(k_z, \Delta z, \omega)^+ + \epsilon} \quad 14$$

where ϵ is a small positive number. In equation 6, the deconvolution estimate can be seen as a gain correction applied to the crosscorrelation estimate. The denominator is the power of the source wavefield and is called the illumination.

METHODOLOGY

In this section I will discuss in brief the methodology and the procedures. The simplified and detailed flow chart shown in figure 1 and 2 respectively highlight the methodology, broadly categorized into five stages namely, model building, zero-offset exploding reflector post stack migration and common-midpoint poststack time and depth migration, prestack depth migration and lastly, iterated poststack and prestack migrations. I will also give a brief data description of the velocities and the seismic datasets generated as well as migrating based on deconvolution and cross-correlation imaging condition.

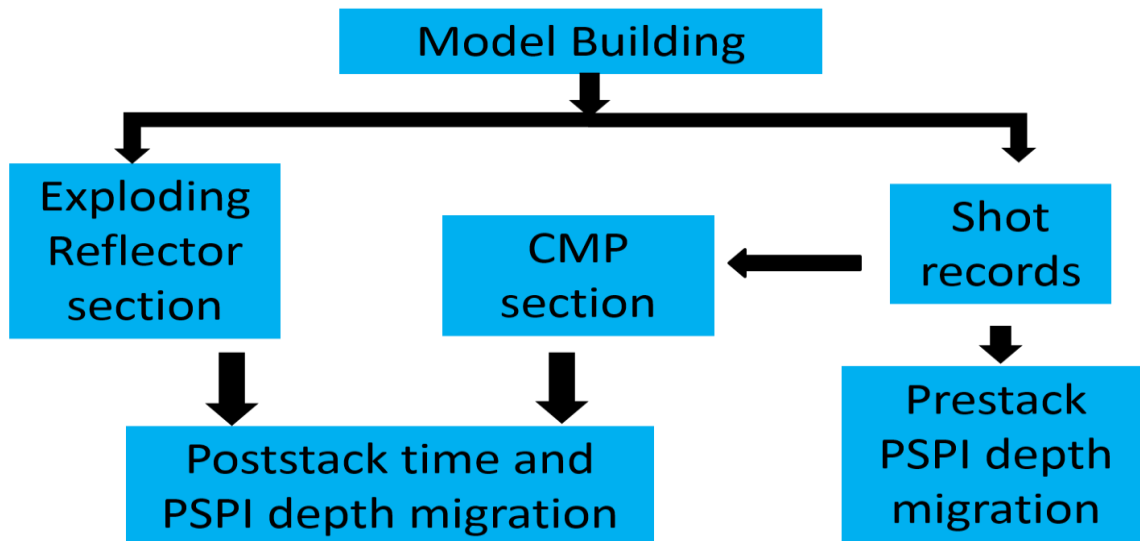


FIG.1. Flowchart of methodology in brief.

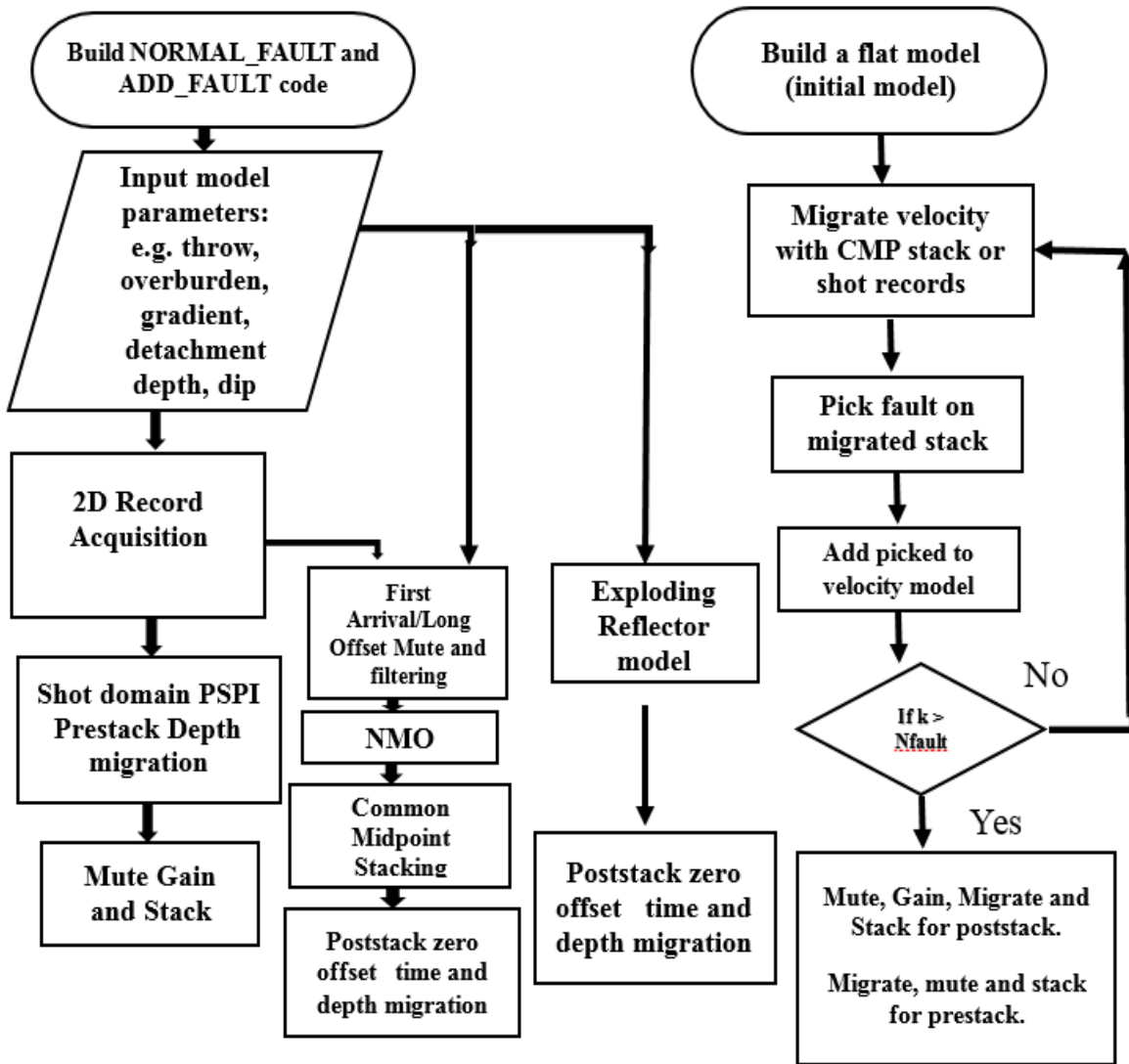


FIG. 2. Full details of study approach involving model building, zero offset and multi-offset seismic acquisition, routine processing and iterated migration.

Data description

The first task of this project was to build a prior and plausible geologic framework that is consistent with real scenario. The geologic model (shown in figure 3 and 4) has a dimension of 10km horizontal offset and 3.8km depth. It is built from a 1D sonic log of 3.75km depth and consisting of few sections of thin layers of low velocity sandwiched within generally increasing velocity medium. The 1D interval velocity log is populated throughout the extent of the model. The velocity grid file was sampled into a 5m (horizontal) by 5m (depth) grid. The size of the velocity grid file is 761 x 2001. I build three listric faults into the model, the velocities in each section of the fault are related to the other section by the throw of the fault. The model parameters including the fault dip, overburden velocity gradient, detachment depth are flexible to change. The geologic model is of flat stratigraphy and continuous except at the fault. The stratigraphy drops 300m to the left of each listric fault which outcrops at 5km, 7km and 9km in the horizontal axis. It cuts through all layers except the top and bottom layer. The velocities and thickness of the layers across the fault remain unchanged.

The two way time conversion of the depth-velocity model reveals time distortion which appear as time sags and pull up. The sharp velocity contrast across the fault will cause seismic waves propagating through this interface to undergo some sort of ray bending and travelttime distortion. The time distortions are confined to the region below the truncation

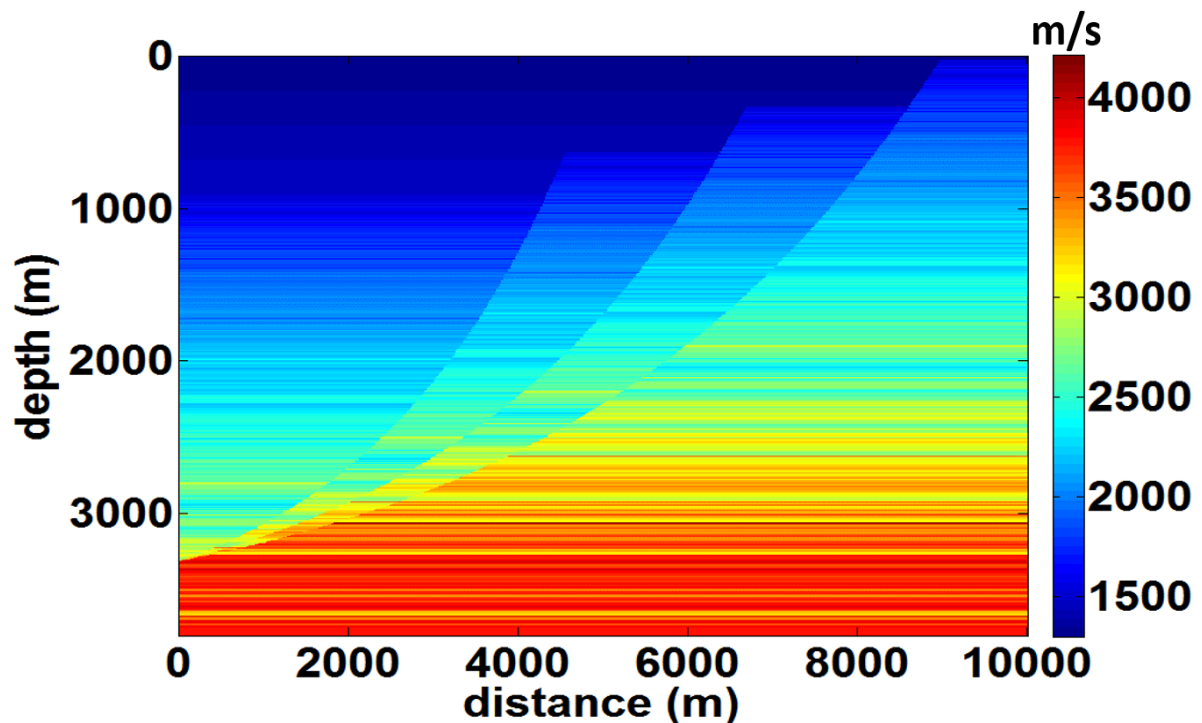


FIG.3. True geologic model (top) and two-way time velocity model (bottom) obtained from depth to time computation.

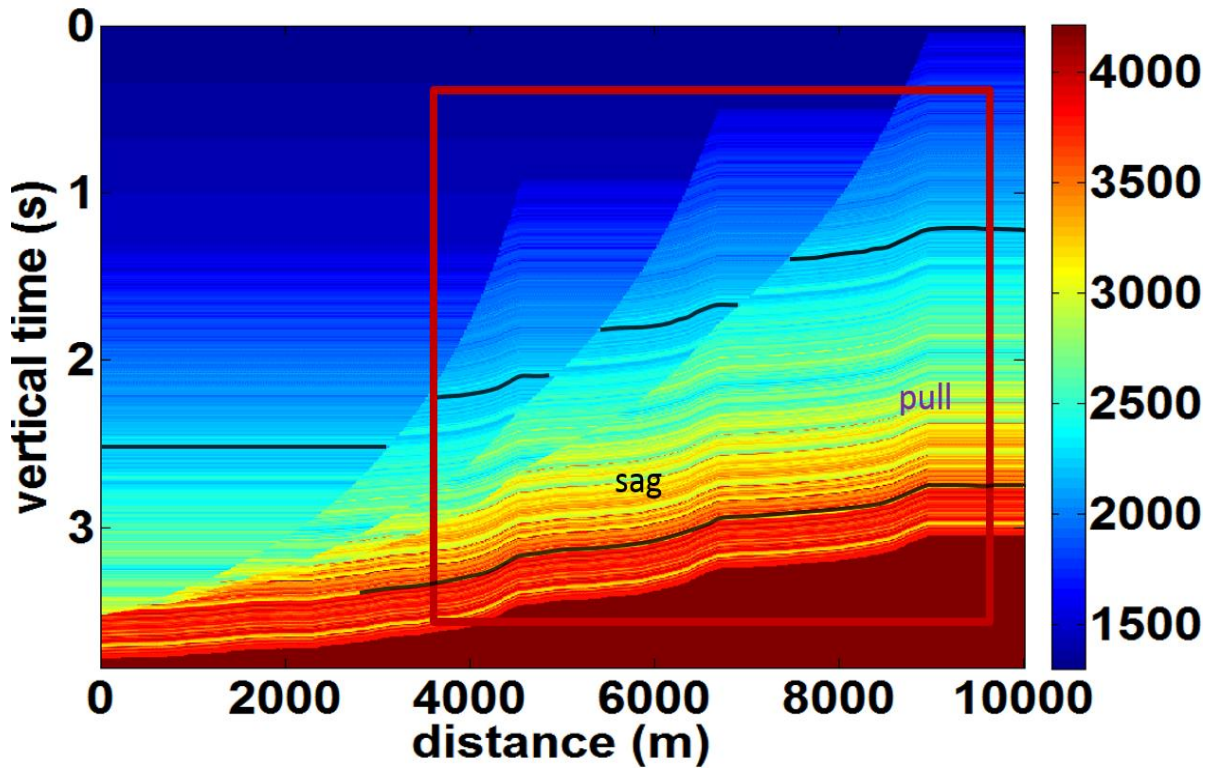


FIG.4. Time distortions behind the fault extends into the footwall of faults and appears as time pull up and sags.

of the overlying stratigraphy by the fault throw thereby causing a strong lateral and vertical velocity contrasts across the fault. The pull up effect can be seen in the vicinity of each fault truncations while the sags can be found in-between consecutive fault truncations. Incorrect positioning of the stratigraphy in time is due to the positioning error of depth to time transformation of the bent image ray to a wrong vertical time.

The 2D velocity models in figure 5a and b show a 2D flat model and a succession of fault updated velocity models for each iterations. However, the closeness of the final approximate model to the true model is largely dependent on the choice of initial starting velocity model used to create the 2D flat model and also on how the faults is picked. The idea behind using these approximate models is to compare the result obtained from migrating with true velocities with those from approximate velocities where information about the true geology is beyond reach.

The velocity model is built from an actual sonic log in order to simulate the geology and to model the cause of shadow zone. Figure 6 is a typical structure in real case example of a major growth boundary fault with oil and gas traps behind the fault. These low velocity anomalies create the pull up and push down effect seen on real seismic dataset (Stuart, 1999). I have not yet introduced such anomalies into my model.

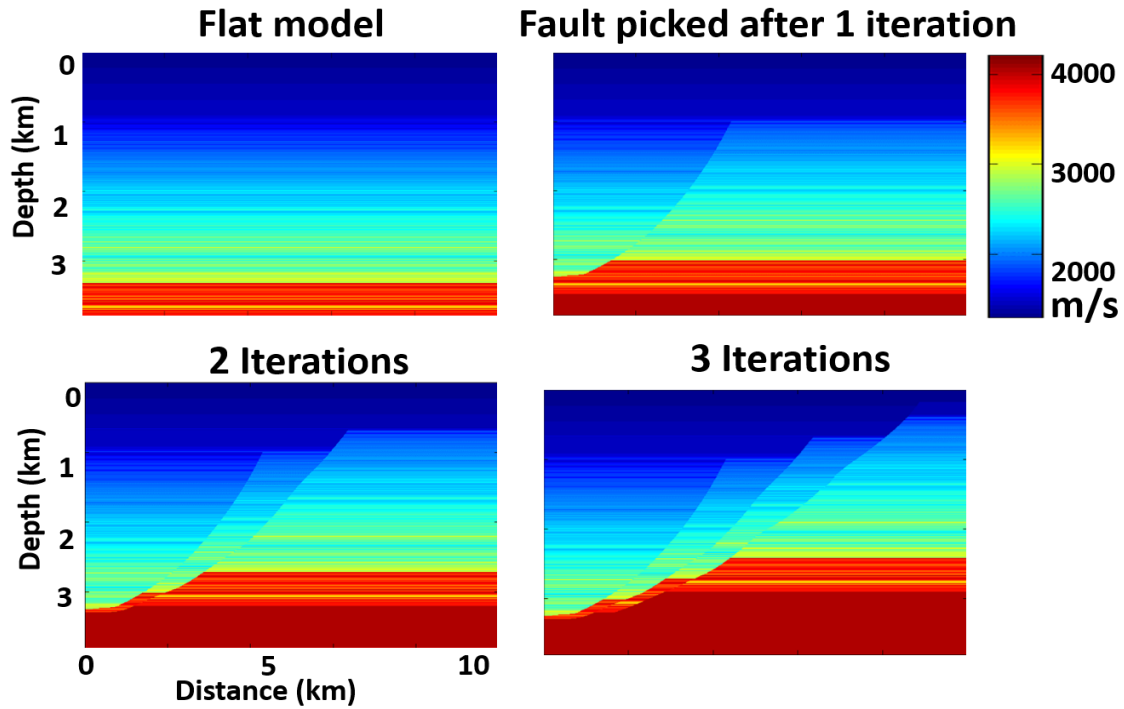


FIG. 5a. Fault constrained velocity building from a flat stratigraphic initial model (top left) and fault updates from each iterations.

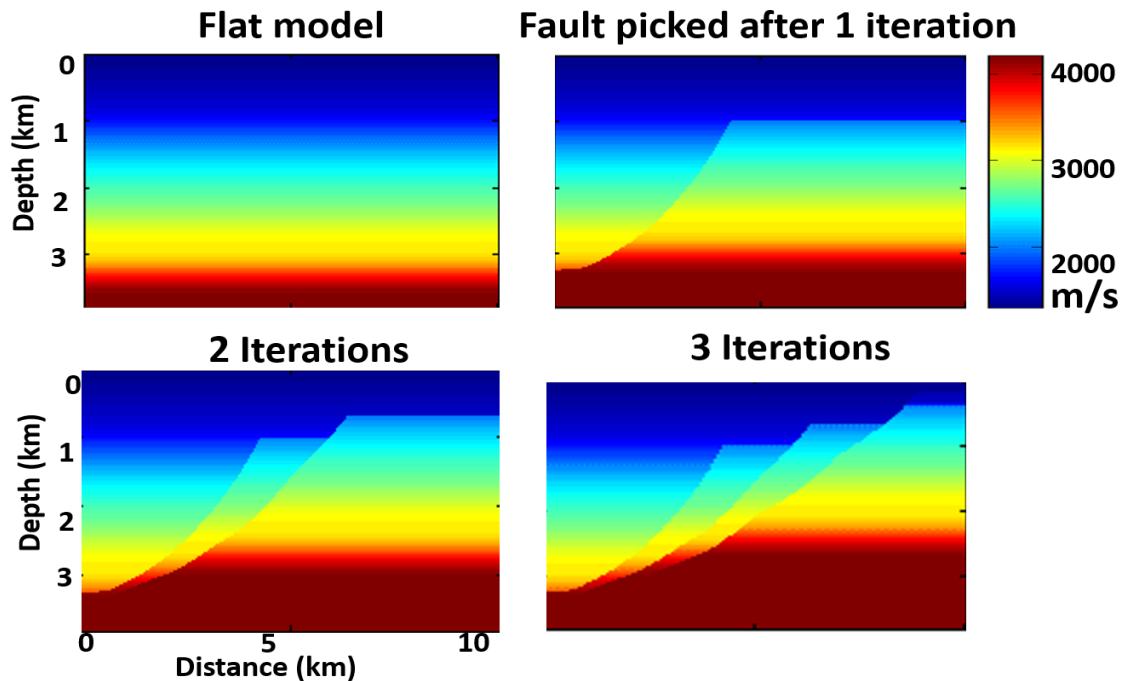


FIG. 5b. Fault constrained velocity building from a Gaussian-smoothed flat initial model and fault updates from each iterations.

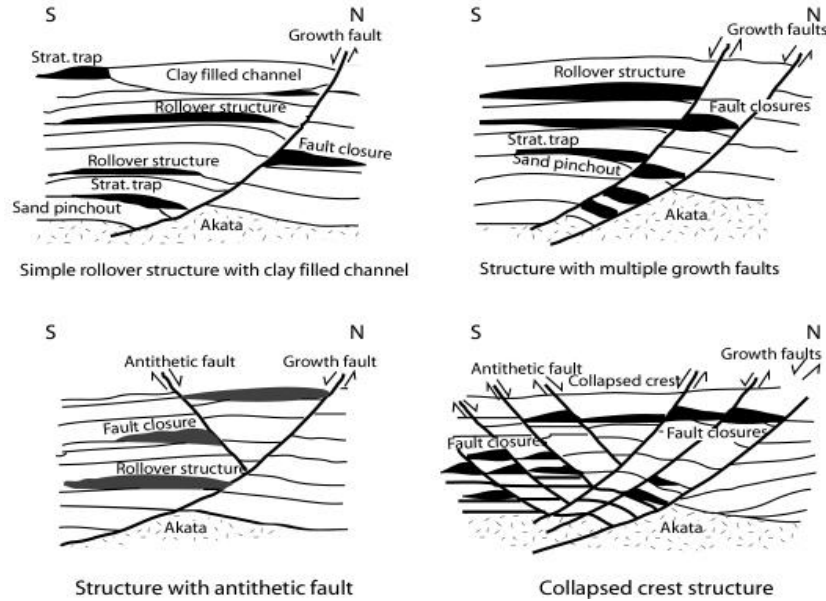


FIG.6. Typical fault structure and associated trap in Gulf of Guinea (Doust and Omatsola, 1990)

A total of 40 synthetic shots were acquired over the 10 km model space, starting from coordinate 500m and ending at 9500m, at an interval of 225m and a receiver spacing was at every 5m. Each shot has receivers across all the model. The source function was a 30 Hz minimum-phase wavelet. The time sampling interval was 4ms and the record length was 5 seconds. The total number of CMP's is 2001 is with a nominal fold of 80. I have not incorporated random noise into the model.

The finite-difference forward modeling used a fourth order spatial approximation which gave shot records with less numerical dispersion and more stability, however the runtime was very high as it took averagely 45 minutes to complete a shot. Figure 7 shows the synthetic shot records and the source wave function. Basic assumptions in the processing of the shots are: (1). No anisotropy and mode conversion (2.) the effect of noise is minimal after applying a mute. The shot records were gained and muted after NMO correction with an rms velocity computed from interval velocity using the hyperbolic travel-time equation. The zero offset common midpoint stack obtained after correcting for the normal moveout time was poststack migrated. The zero-offset exploding reflector section is poststack migrated similarly.

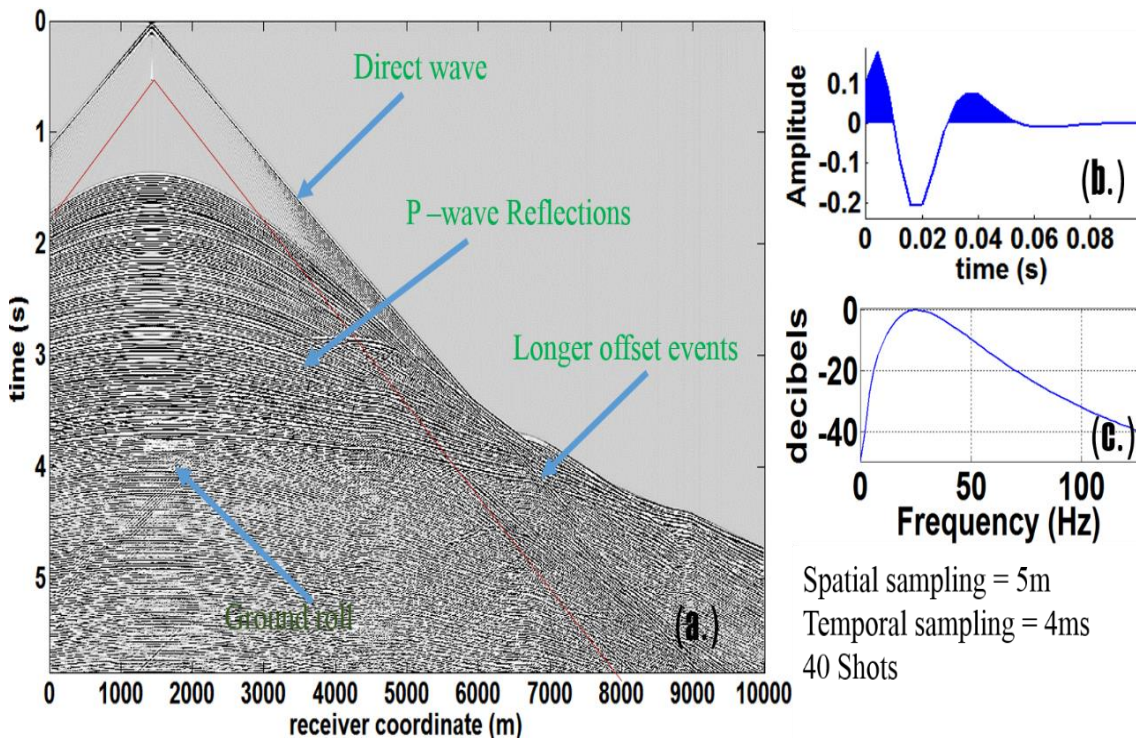


FIG.7. A clipped shot record (a) and source wavelet (b)

The shot records were then migrated with the shot-type PSPI algorithm and imaged using the deconvolution and cross-correlation (Claerbout, 1971) imaging conditions. The whole procedure for zero-offset poststack time and depth migration and the shot-domain prestack migration steps were repeated in the iterated migration scheme starting with a flat velocity initial model and migrating for each fault update. The results shown in figure 8 are the stacked sections of the shot domain PSPI migration using Claerbout's 1971 deconvolution and crosscorrelation imaging conditions (equation 13 and 14).

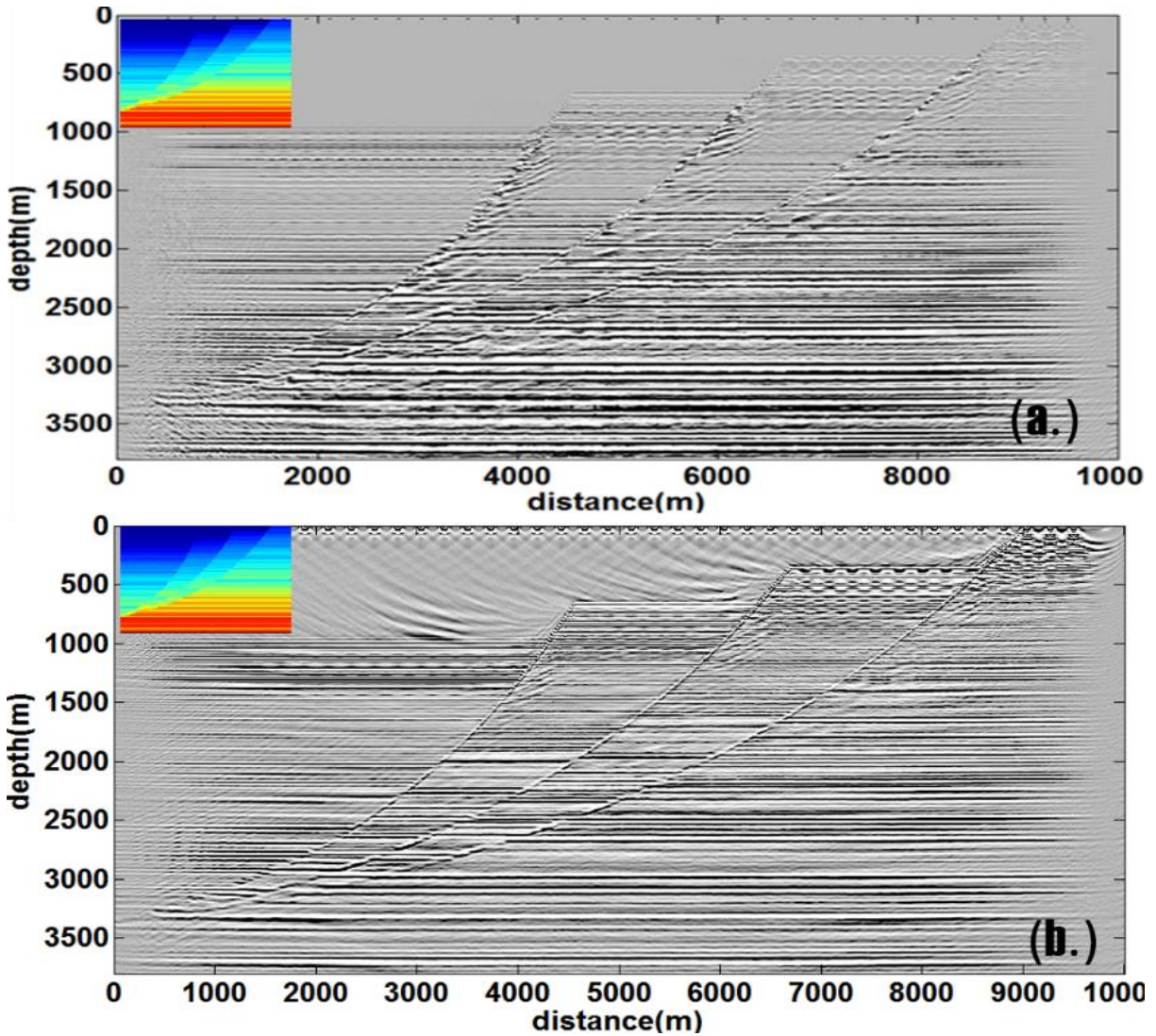


FIG.8. Prestack depth migration of true model using Claerbout's imaging conditions, deconvolution imaging condition (a) and crosscorrelation imaging condition (b). The footwall reflections are better imaged than for post stack time and depth migrations of the true model.

Figure 8b is the result of cross-correlation imaging condition, the advantage of this over the deconvolution imaging condition is its suppression of migration artifacts and is the point of reference for imaging condition that includes illumination compensation. Subsequent migration results will show only the cross-correlation images.

The result obtained from the prestack depth migration give credence to the capability of prestack depth migration in imaging behind fault of this nature. Reflectors behind the fault were correctly imaged. The fault image obtained from the deconvolution imaging condition appeared blurred, a reason for this being the existence of residual migration noise. This was mitigated by applying a more severe mute to the migrated shots. In subsequent prestack depth image results, I will show prestack results from the cross-correlation imaging condition only.

RESULTS

This section explains the results the zero offset and shot-domain time and depth migrations, first with the actual geology known and followed by migration results obtained from guessed velocities.

Poststack Time Migration

Figure 9 below shows the rms velocity used in the poststack time migration. The exploding reflector model migration results (figure 10) and post stack time migration result in figure 11 show that time migration is able to image the section of the hanging wall not in the shadow of its neighbouring fault, but extremely limited in imaging the footwall as seen by the distorted reflections. This will make it difficult for an inexperienced interpreter to make out any meaningful analysis from the time migrated faults. The solution by poststack migration for faulted geology of this kind is near if accurate NMO and DMO corrections are applied. The present of fault even in a simple model introduces anisotropy and creates non-hyperbolic moveout which may cause classic NMO correction to fail. The exploding reflector time migrated section is much better than its' cmp-poststack as we would expect because the CMP-stack is not perfectly a zero offset section compare to the normal incident reflection of the exploding reflector model. Also the dip dependence of stacking velocities will cause a lesser quality zero-offset stack. Furthermore, without the knowledge of fault shadows on seismic datasets, it is easy to misinterpret the distorted footwall reflectors seen on the migrated section in figure 10 as another subseismic fault with conflicting dip or as a back to back fault.

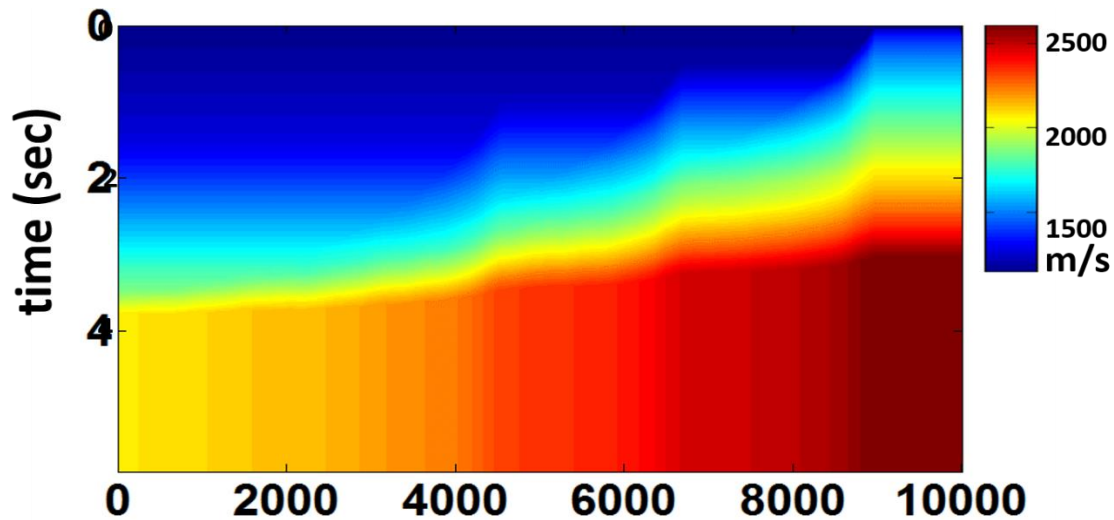


FIG.9. Root-mean-square velocity used in time migration.

Another factor why the footwall reflectors in common-midpoint time migration is severely distorted is because RMS velocity is severely limited by the image ray characteristics of ray bending as it travels from the overburden through fault truncations.

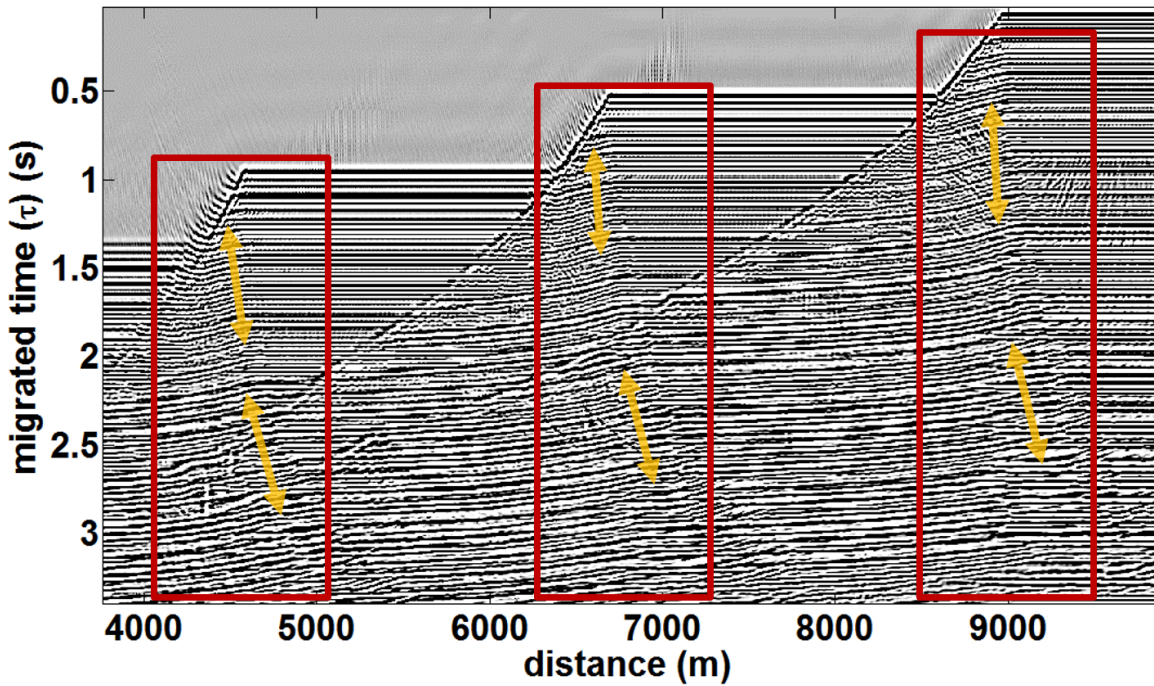


FIG.10. Poststack time migration of exploding reflector model

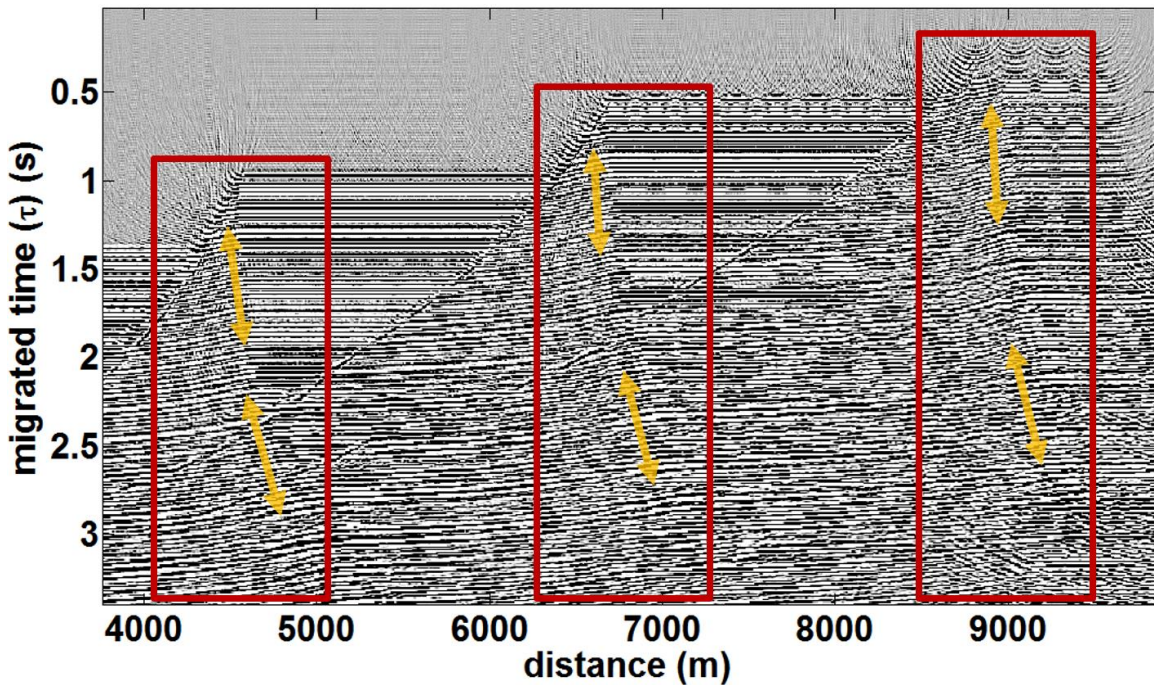


FIG.11. Poststack time migration of common midpoint stacked section

Post and Prestack Depth Migration with exact velocity

The results from this section show images from three depth migrations with an exact velocity namely: exploding reflector depth migration (figure 12), CMP poststack depth migration (figure 13) and shot domain prestack depth migration (figure 14). Even though the results are fairer than those obtained from poststack time migrations, Common

midpoint poststack depth migration gave the most distorted footwall image in this section. The reasons are not farfetched. Poststack depth migration without dip moveout correction does not properly migrate footwall reflections to their correct location. This anomaly is the cause of the “smiles” in the common midpoint depth migration shown in figure 13. Because of the incorrect stacking velocities used to nmo-correct the shot records, the final results of cmp-poststack migration is affected. Prestack result show a well-imaged footwall because a prestack is synonymous to a poststack plus dip-moveout (Bancroft course note 2014). For CMP stacking, we normally assume hyperbolic moveout. In the presence of lateral velocity variations at the fault truncations as well as the presence strong vertical and lateral heterogeneity of the layer velocities, the hyperbolic assumptions may not hold. The assumption that a conventional stacked section is equivalent to a zero-offset section is also violated to a varying degree in the presence of dipping faults (Yilmaz, 2001), thus poststack depth migration fails. When velocity variation (particularly those associated with abrupt changes caused by fault truncation or layer velocity thickness) give rise to reflections with non-hyperbolic moveout, time imaging and poststack depth imaging will fail behind the faults. Figure 13 shows that prestack depth imaging resolve aspects of the structure beyond the reach of poststack depth imaging.

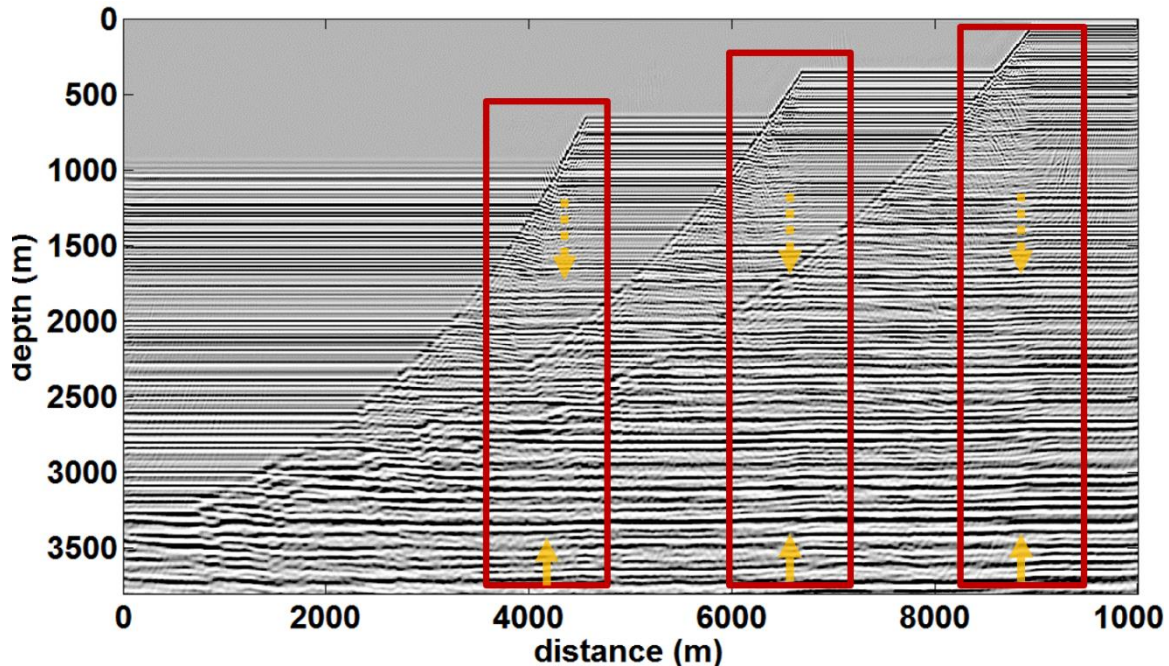


FIG.12. Poststack depth migration of exploding reflector model with exact velocity.

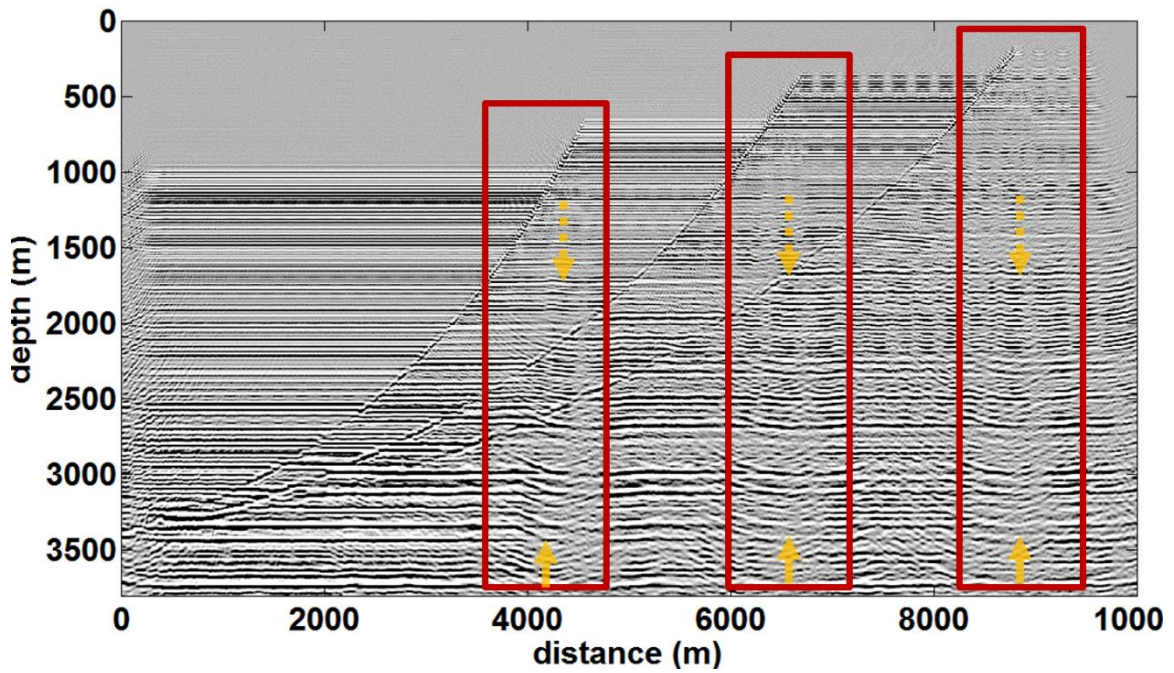


FIG.13. Poststack depth migration of common midpoint stacked section with exact velocity.

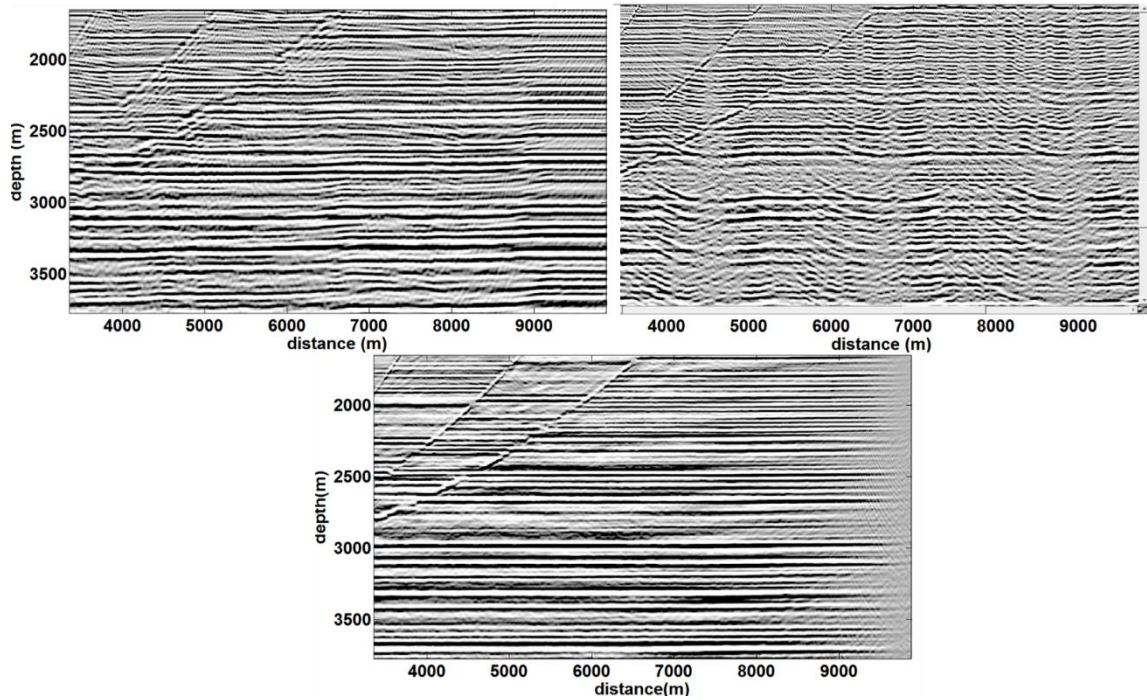


FIG.14. detailed comparison of depth images (a). Exploding reflector, (b). Poststack migration and (c). Prestack migration

Iterative migration with exact velocity

The aim of the iterated migration was to simulate a real case scenario fault shadow processing. In this section we assume the geologic model is not given. We start with a trivial velocity model (figure 5a) and iteratively build into the trivial model co-ordinates of fault picked from a stacked seismic section so as to obtain a final model that is closer to the true model. Figure (15 -19) discussed in this section refer to post stack depth migrations starting with a trivial flat initial model, updating new picks into the velocity model until I have obtained a final velocity with updates from all the three faults seen on the seismic section. I also show here a final poststack depth and a first-time prestack depth migration of the final approximate model.

We can see from the iterated poststack depth migrations that post stack migration is limited in imaging behind faults, we can also notice that migration with the approximate velocity models show susceptibility of poststack migration of highly faulted geologic environment to fault shadows. Footwall reflection deteriorates with further updating of faults into approximate models. In addition, the prestack depth image is not completely free from fault shadow effect as seen in figure 19 by the yellow, we see a narrow region of conflicting reflection extending from the throw to the bottom of the second and last fault in the depth image.

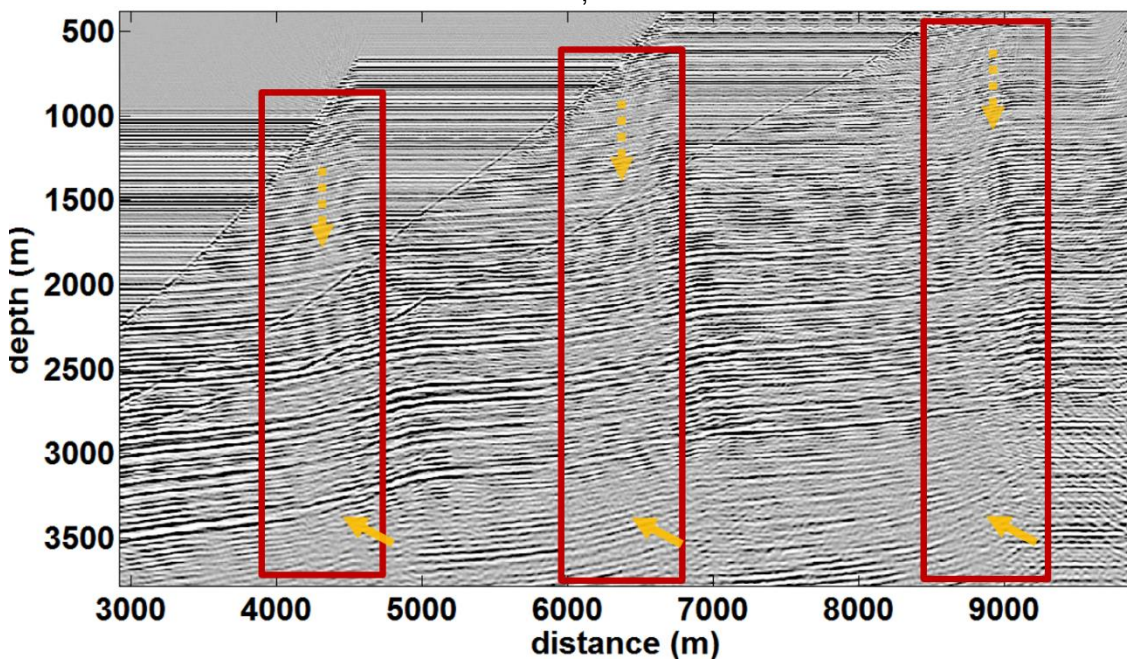


FIG.15. Poststack depth migration with fault constrained exact velocity from flat velocity

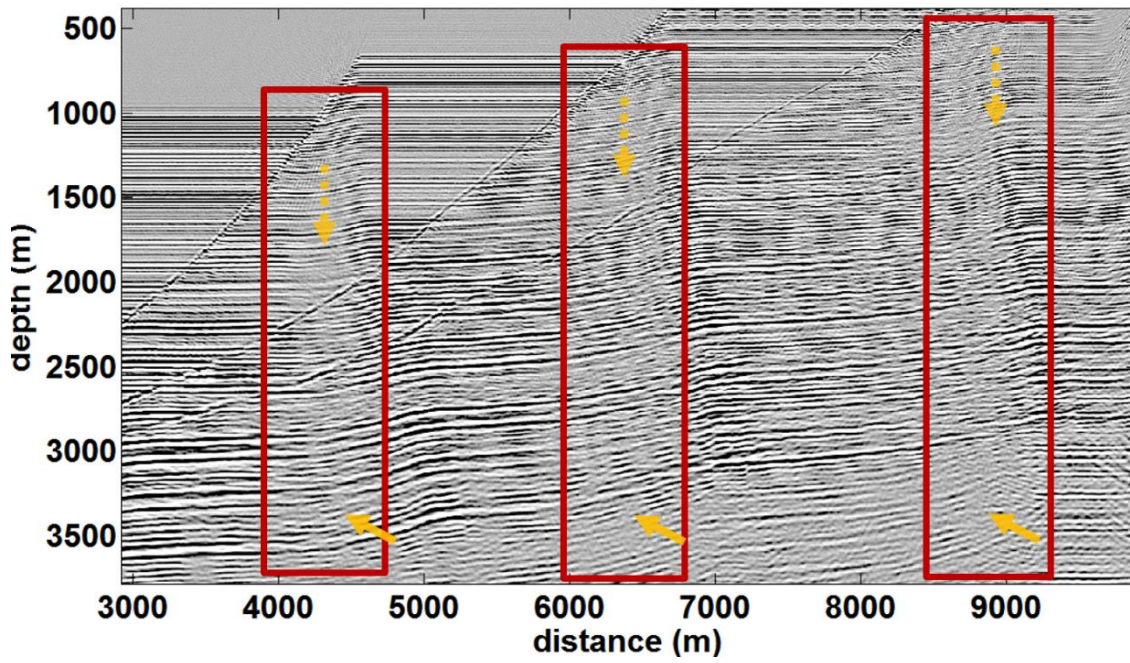


FIG.16. Poststack depth migration with fault constrained exact velocity from first fault pick

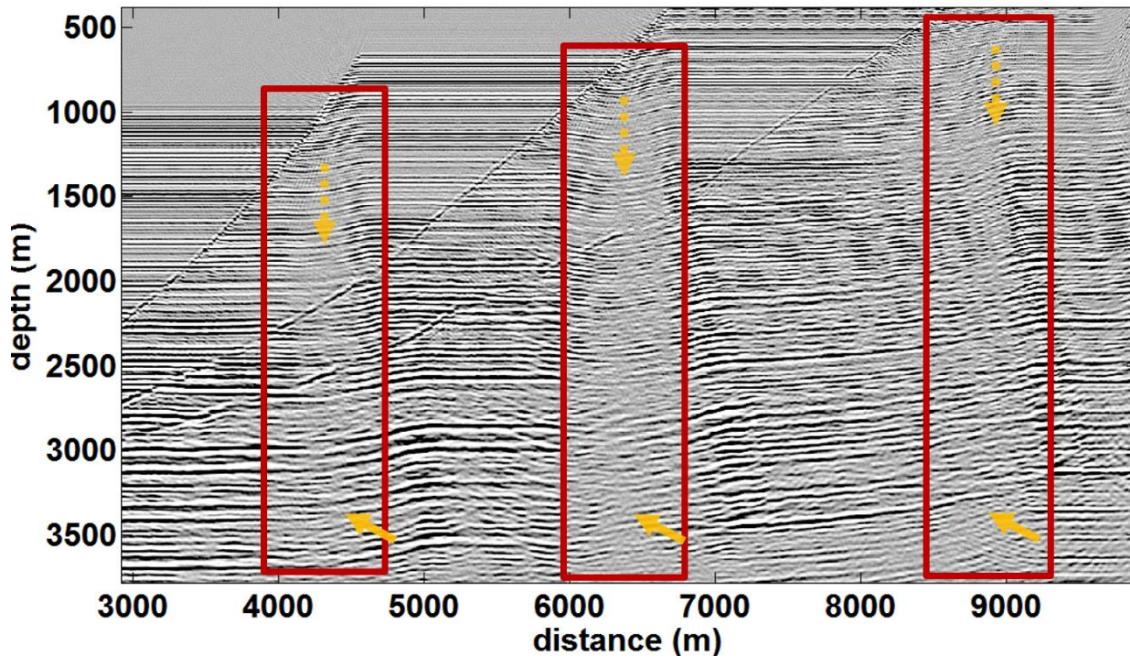


FIG.17. Poststack depth migration with fault constrained exact velocities from second fault pick

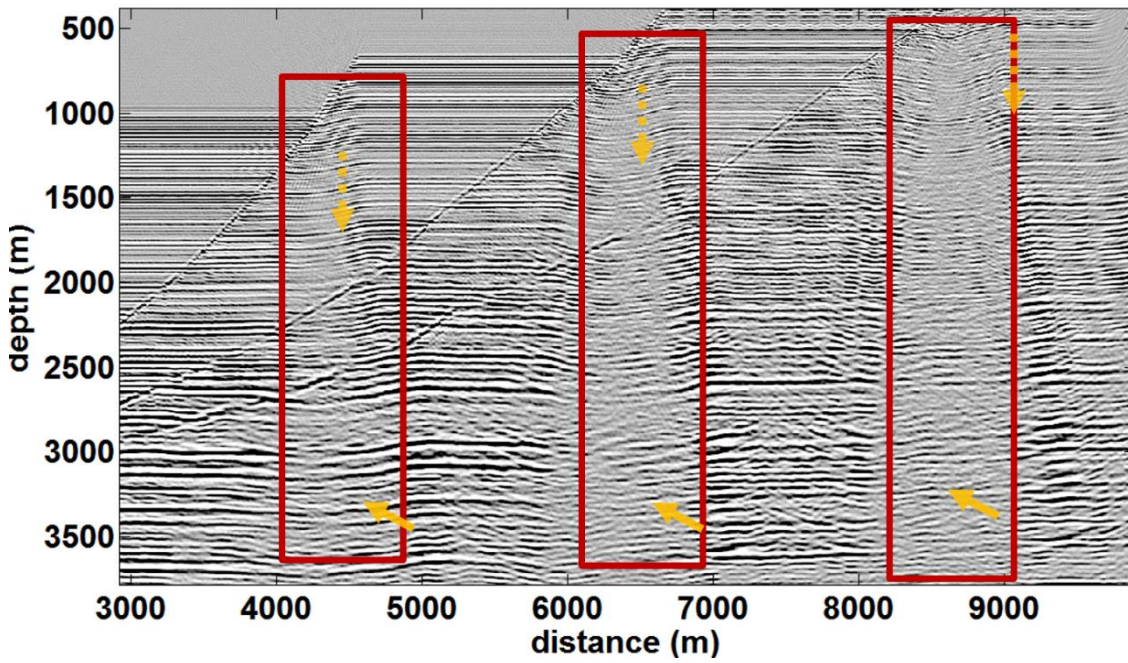


FIG.18. Poststack depth migration with fault constrained exact velocities from final fault pick

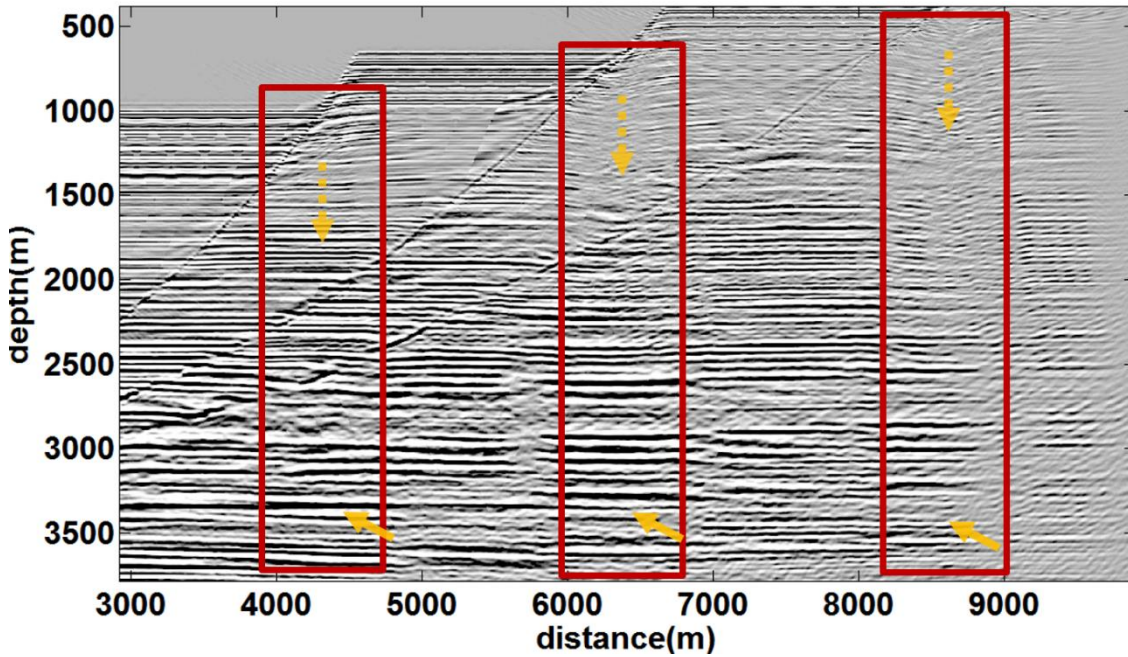


FIG.19. Prestack depth migration with final iterated exact velocities

Iterative migration with smooth velocity

The same effect observed in the previous section is also observed in this section. The false anticlines and synclines also occur in the iterated poststack depth images obtained from iterated migrations (shown in figure 20 - 24) with the smooth approximate velocities of

figure 5b. As before, the reflectors become flat beneath the footwall in region outside the heaves of the faults. Reflectors located within the heaves and the throw of the faults appear as sequence of synclines and anticlines in the poststack depth image while the footwall reflectors in prestack is improved. The fact that the prestack migration do not show a clear fault shadow characteristic, means that fault shadow can be resolved with prestack depth migration using accurate migration velocities.

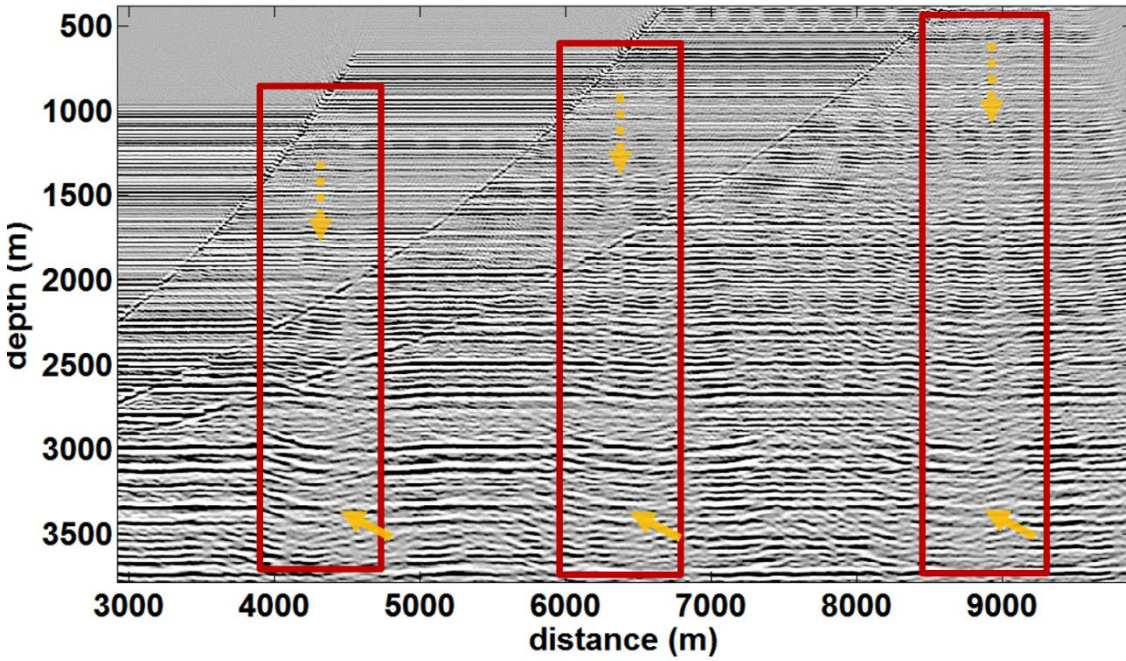


FIG.20. Poststack depth migration with fault constrained smoothed velocity from flat velocity

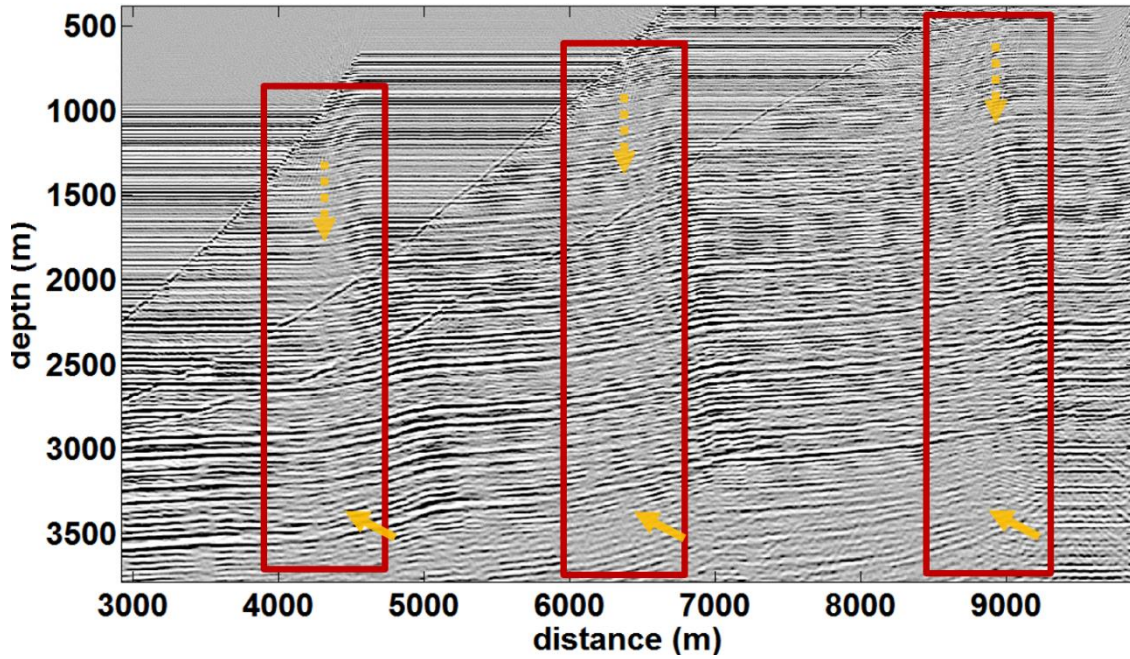


FIG.21. Poststack depth migration with fault constrained smoothed velocity from first fault pick

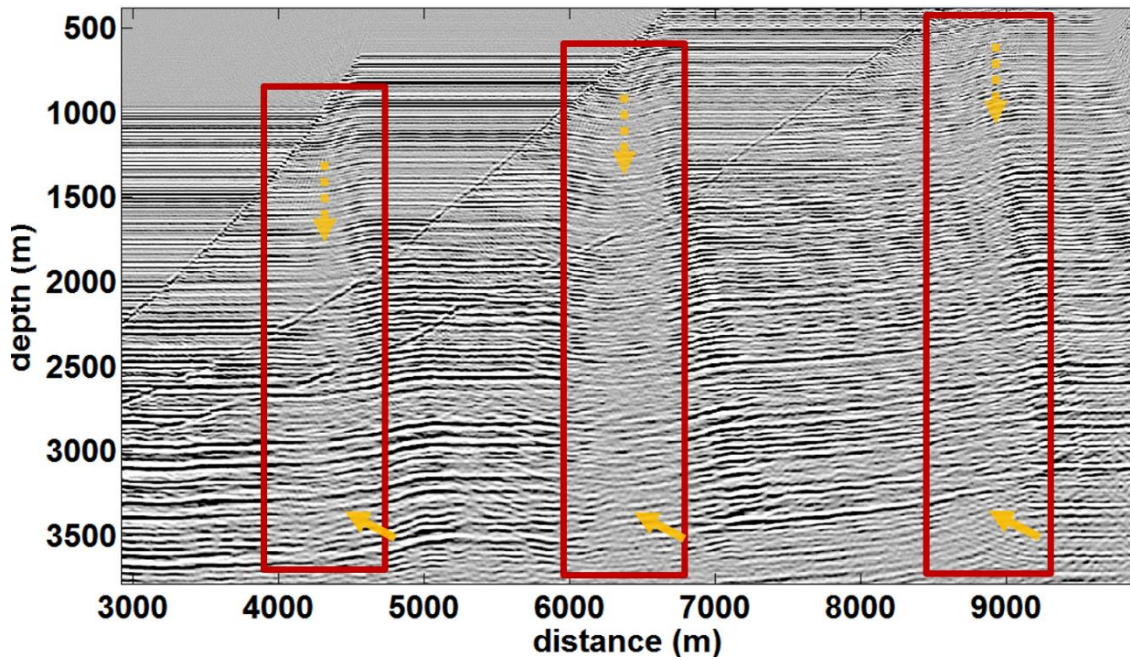


FIG.22. Poststack depth migration with fault constrained smoothed velocity from second fault pick

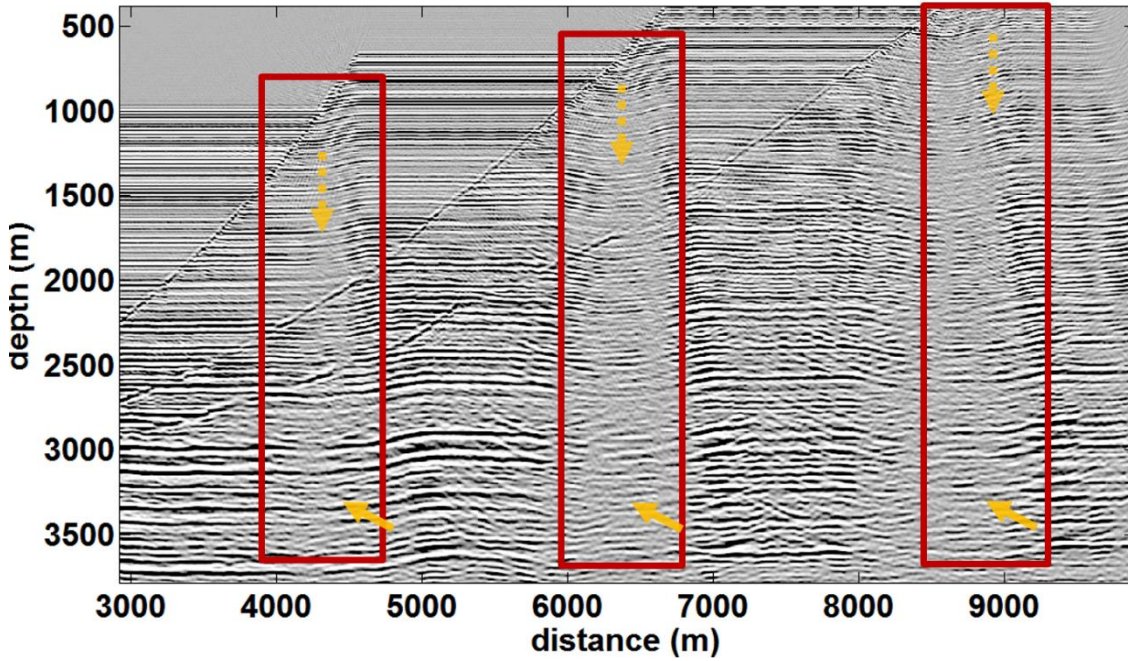


FIG.23. Poststack depth migration with fault constrained smoothed velocity from final fault pick

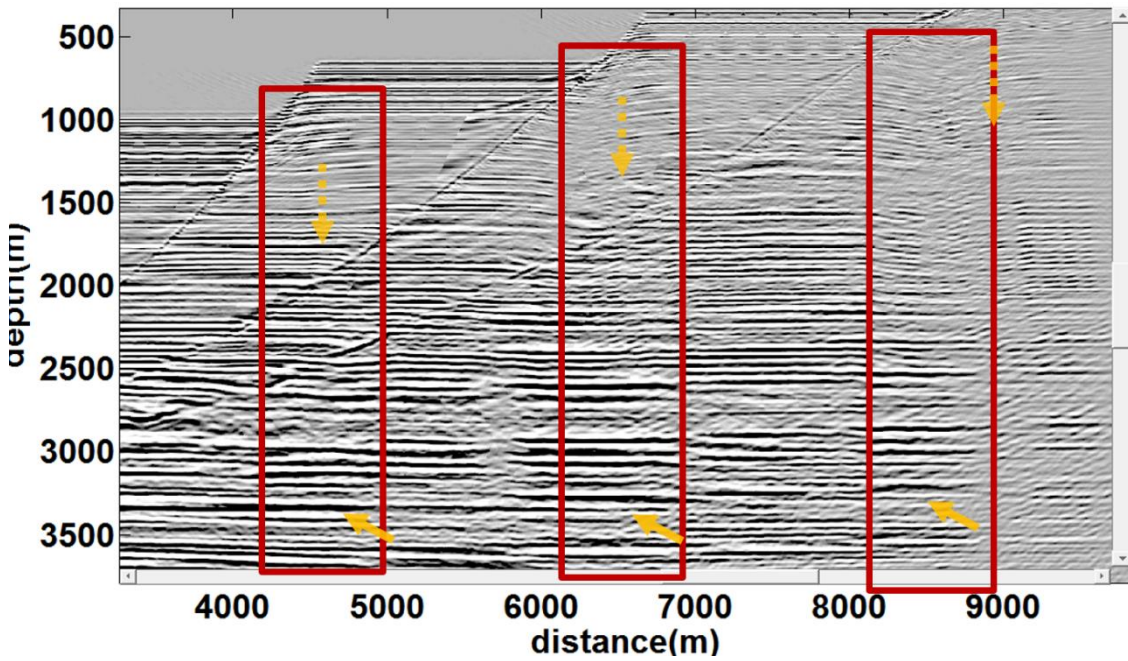


FIG.24. Poststack depth migration with final iterated smoothed velocities

Comparing all the results from each section we can see that the seismic distortions and the poor illuminations behind faults, majorly conspicuous in post stack migrations, are as a result of the truncation of the overlying stratigraphy by the fault throw causing velocity contrasts across the fault. Limitations of time migration causes wrong alignment of images in time. The second primary cause of the disrupted reflections are non-hyperbolic moveout nature of faults and footwall reflectors. Their hyperbolic nature is related to relative

advancement or delays at offsets with respect to near as the gather straddles the fault. For CMP stacking, we normally assume hyperbolic moveout. In the presence of lateral velocity variations at the fault truncations as well as the presence strong vertical and lateral heterogeneity of the layer velocities, the hyperbolic assumptions may not hold. The assumption that a conventional stacked section is equivalent to a zero-offset section is also violated to a varying degree in the presence of dipping faults (Yilmaz, 2001), thus poststack depth migration fails. When velocity variation (particularly those associated with abrupt changes caused by fault truncation or layer velocity thickness) give rise to reflections with non-hyperbolic moveout, time imaging and poststack depth imaging will fail behind the faults. Another factor that may cause the poor imaging in the poststack migration if not account for is the effect of dip dependence of normal moveout. NMO and stacking of events along hyperbolas without prior dip moveout correction of dipping data will cause apparent disruptions and smeared reflections. The figures already discussed above shows that prestack depth imaging can resolve aspects of the structure beyond the reach of poststack depth imaging.

CONCLUSION

The causes of fault shadows and the capabilities of poststack and prestack migration in imaging listric faulted geology has been looked into from a 2D seismic modeling view point. The following conclusions can be drawn: - (1). Shadow zones should be expected in faulted geology where strong velocity variation occur at fault termination. Fault shadow time anomalies are subtle typically in tens on milliseconds. The low illumination in the footwall becomes more evident with each iterations, this confirms the hypothesis that fault shadow is majorly a velocity problem. The presence of these dipping faults creates non-hyperbolic moveout, these causes seismic processing which depend on moveout assumptions to fail. (2.). Results from the post-stack migrations are severely affected by the dip limitations in the stacking process and of the zero-offset migration and thus are not effective in completely imaging footwall reflections. (3). Lastly, We can see that prestack depth migration is far more promising in handling imaging challenges associated with faults than poststack depth migration. In the future, I will build a more geologically consistent fault model, and stretch the capability of depth migration in migrating footwall reflection using an effective migration velocity model in a more realistic scenario. I will also incorporate seismic attenuation and anisotropy.

ACKNOWLEDGEMENT

The authors would like to acknowledge CREWES sponsors and NSERC (Natural Science and Engineering Research Council of Canada) for providing the financial support for this research.

REFERENCE

Allen, J.L. and L. J, Bruso, 1989, A case history of velocity problems in the shadow of a large growth in the Frio formation, Texas Gulf Coast: *Geophysics*, **54**, pp. 426–439, doi:10.1190/1.1442668

Aikulola, U. O, S.O. Olotu, and Yamusa. I., 2010 , Investigating fault shadows in Niger Delta, TLE.

Bagaini, C., E. Bonomi, and E. Pieroni, 1995, Data parallel implementation of 3D PSPI: 65th Annual International Meeting, SEG, Expanded Abstracts, 188–191.

Bancroft J.C., 2007., A Practical Understanding of Pre- and Poststack Migrations, Volume 1 (Prestack), SEG Course Notes Series No. 14, Society of Exploration Geophysicists, Tulsa, OK.

Bancroft J.C., 2014, Seismic Imaging Theory Course note, University of Calgary

Birdus, B., 2007, Removing fault shadow distortions by fault-constrained tomography, SEG Technical Program Expanded Abstracts 2007: pp. 3039-3043. doi: 10.1190/1.2793102.

Claerbout, J. F., 1971, Towards a unified theory of reflector mapping: *Geophysics*, 36, no. 3, 467-481.

Doust,H. and E.M. Omatsola, 1990, Divergent and Passive Margins. AAPG Memoir, N0 48, p.201-238.

Fagin, S., 1996. The fault shadow problem: Its nature and elimination: *The Leading Edge*, 15, 1005–1013, doi: 10 .1190/1.1437403.

Ferguson, R. J., and G. F. Margrave., 2005. Planned seismic imaging using explicit one-way operators: *Geophysics*, 70, no. 5, S101–S109.

Gazdag, J., and P. Sguazzero, 1984, Migration of seismic data by phase-shift plus interpolation: *Geophysics*, 49, 124–131.

Hardwick A.J, Rajesh L. 2013,A 3D Illumination Study to Investigate Fault Shadow Effects over the Hoop Fault Complex, 75th EAGE Conference & Exhibition incorporating SPE EUROPEC 2013.

Krebes, E.S., Quiroaa-Goode, G.: A standard finite difference scheme for the time-domain computation of anelastic wavefields. *Geophysics* 59, 290–296 (1994).

Manning, P. M., and Margrave, G.F., 1999, Finite difference modelling as a practical exploration tool, CSEG Convention Abstract, P.240-243.

Schultz, P., 1999, The seismic velocity model as an interpretation asset, SEG Distinguish Instructor Short Course, Series, No.2

Yilmaz, Öz (2001). *Seismic data analysis*. Society of Exploration Geophysicists. ISBN 1-56080-094-1.

Youzwishen, C.F., and G.F. Margrave, 1999, Finite Difference Modelling of Acoustic Waves in MATLAB: CREWES Report, 11.

APPENDIX

```

%% Build a normal fault 2D velocity model from 1D velocity file
xmax=10000; % model length
zmax=3759;% model depth
dx=2.5;%spatial sampling
modelname='Normal faults';% model name
dzblk=dx;%log depth step
dzout=dx;%Output sample rate of logs
vp0=1700;
throws=[900 600 300];%fault throw
xfaults=[5000 7000 9000];%x-cordinated of fault outcrop
% vpblk vector of p-wave velocity
vector of depths sampled at log depth step
v0=1300;% is overburden velocity at z0(first logged depth)
c=0.8;% is overburden velocity gradient
dipfactor=4;% controls the steepness of the fault
%
[vpblk,vsblk,rhoblk,zblk,z0]=blocklogs('gbaran_002logedit.las',dzblk,dzout,vp0
,vs0,rho0);
% ind=near(zblk,z0);
[vel,x,z]=normal_faults2(dx,xmax,zmax,xfaults,throws,z0+throws,vpblk(ind(1):
end),zblk(ind(1):end),v0,c,dipfactor);
vmin=min(vel(:));
vmax=max(vel(:));
%
figure
imagesc(x,z,vel);colorbar; title('Normal fault velocity model')
xlabel('distance (m)');ylabel('depth (m)')
prepfig

```

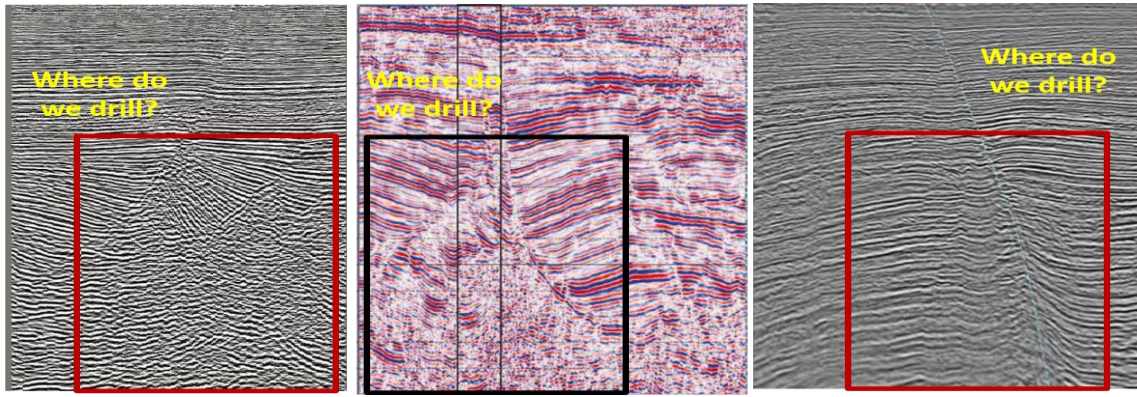
Appendix I. A sample code for building a normal fault velocity model

```

%code to add fault to a velocity model
c=.001;v0=1250;
load pick % load previous picks
% [xf1,zf1]=ginput(10);
throw=300;
velj1=addfault2(velflat,x,z,xf1,zf1,throw,c,v0);

```

Appendix II. A sample code to pick fault on a display and update pick into a velocity model



Appendix III. (a) Kirckhoff depth migration of the South Texas (Bednar et.al. 2003), (b). Conventional PSDM of the Gulf of Guinea (aikulola et.al. 2010) and (c). common offset poststack depth migration of the Permafrost of Siberia Quigley et.al. 2012).